

Full length article

Determination of crustal thickness under Tibet from gravity-gradient data



Wenjin Chen*

School of Geodesy and Geomatics, Wuhan University, 430079 Wuhan, China

Department of Mathematics and Geosciences, University of Trieste, 34127 Trieste, Italy

ARTICLE INFO

Keywords:

Moho geometry
Gravity-gradient
Crustal thickness
Tibet

ABSTRACT

We develop a novel regional inversion algorithm to determinate the Moho geometry from the gravity-gradient data. The procedure involves two steps. Firstly, the refined gravity-gradient data, which comprise mainly the gravitational signal of the Moho geometry, are obtained from applying the gravimetric forward modeling by using a tesseroid method. Secondly, the refined gravity-gradient data are used to find the Moho depth. The functional relationship between the (known) refined gravity-gradient data and the (unknown and sought) Moho depth is defined by means of the (nonlinear) Fredholm integral equation of the first kind, which is further linearized by means of applying a Taylor series. To stabilize the inverse solution of the system of observation equations, the Tikhonov regularization is applied. The developed algorithm is tested at the study area of Tibet characterized by the largest crustal thickness. Results of the gravimetric inversion (for the uniform and variable Moho density contrast models) have a relatively good agreement with the seismic model (CRUST1.0) at the level of expected uncertainties of about 5 km without the presence of a significant systematic bias.

1. Introduction

The Mohorovičić discontinuity (Moho) is the boundary between the Earth's crust and mantle. The estimation of the Moho parameters (i.e., the Moho depth and density contrast) is commonly obtained from either the seismic or the gravimetric data. However, the applications of seismic methods are still limited by the inadequate seismic data coverage over large parts of the world, including Tibet. Nevertheless, several seismic studies have been carried out in order to investigate the crustal structure of Tibetan (and Himalayan) orogenic formation for a better understanding of the subduction mechanism of the Indian tectonic plate under the Tibetan block. Among the existing seismic studies investigating the crustal structure under Tibet and the Himalaya, studies have been done by Zhao et al. (1993), Stauffer (1993), Zeng et al. (1994, 2002), Nelson et al. (1996), Bump and Sheehan (1998), Kind et al. (1996, 2002), Roecker (2001), Zhang et al. (2011), Gao et al. (2005), Wittlinger et al. (2004), Rai et al. (2006), Vinnik et al. (2006) and Bagdassarov et al. (2011).

In the absence of seismic data, gravimetric methods are often applied to determine the global or regional Moho depth. This is possible especially after launching satellite gravity missions: the Gravity Recovery and Climate Experiment (GRACE) (Tapley et al., 2004a, 2004b) and the Gravity field and steady-state Ocean Circulation Explorer (GOCE) (Floberghagen et al., 2011), which mapping the Earth's gravity field with an unprecedented resolution and accuracy.

Various gravimetric methods for the Moho recovery have been developed and applied. Several contributions could be mentioned by Ye et al. (2016), Eshagh and Hussain (2016), Sampietro (2016, 2011), Shin et al. (2015, 2006), Tenzer and Chen (2014), Van der Meijde et al. (2013), Bagherbandi (2012), Eshagh et al. (2011), Gómez-Ortiz et al. (2011), Sjöberg and Bagherbandi (2011), Sjöberg (2009), Jin et al. (1994) and Moritz (1990).

In this study, we present a novel approach for the determination of the regional Moho geometry from the gravity-gradient data. For this purpose, the gravity-gradient data were generated from the GOCO05S (Mayer-Gürr et al., 2015) coefficients and then used to recover the Moho depth under Tibet with the help of the additional geophysical data and the spectral filtering technique. The significance of using gravity-gradient data to investigate the Earth's crustal structure has already been discussed by e.g., Eshagh (2014) and Sampietro et al. (2014). In order to recover the gravitational signal of Moho geometry from the observed gravity gradients, the stripping corrections are applied to model and remove the contributions of all known anomalous mass density structures within the Earth's crust. Moreover, the mantle density heterogeneities should be taken into consideration as well. The resulting refined gravity field quantities, which have a maximum correlation with the Moho geometry, are theoretically the most appropriate for a gravimetric Moho recovery (cf. Tenzer et al., 2009, 2012c). Therefore, firstly we applied the gravimetric forward modeling (using the tesseroid method) to model and remove the contribution of

* Address: School of Geodesy and Geomatics, Wuhan University, 129 Luoyu Road, Wuhan 430079, China.

E-mail addresses: chenwenjinwhu@gmail.com, [cjw@whu.edu.cn](mailto:cwjwhu@whu.edu.cn).

the crustal density heterogeneities from the observed gravity-gradient data. Then we used the spectral filtering technique to remove the long-wavelength mantle signal (e.g., Bagherbandi and Sjöberg, 2012; Eckhardt, 1983). The developed methodology is summarized in the next section.

2. Methodology

2.1. Gravimetric forward modeling

The computation of the consolidated crust-stripped gravity-gradient data (i.e., the refined gravity-gradient data) was realized according to the following scheme

$$\delta T_{rr}^{cs} = \delta T_{rr} - \delta T_{rr}^t - \delta T_{rr}^b - \delta T_{rr}^s - \delta T_{rr}^c - \delta T_{rr}^{\text{un-modeled}}, \quad (1)$$

where δT_{rr} denotes the disturbing gravity-gradient, $\delta T_{rr}^t, \delta T_{rr}^b, \delta T_{rr}^s$ and δT_{rr}^c are, respectively, the gravitational gradient contributions generated by the topography and density contrasts due to the bathymetry, sediments and anomalous crustal density structure, $\delta T_{rr}^{\text{un-modeled}}$ represents the remaining gravity-gradient contributions attributed mainly to the crustal density model uncertainties and the gravitational signal of deep mantle density heterogeneities.

The components of $\delta T_{rr}^t, \delta T_{rr}^b, \delta T_{rr}^s$ and δT_{rr}^c were computed from the CRUST1.0 seismic crustal model (Laske et al., 2013) and the ETOPO1 topographic/bathymetric data (Amante and Eakins, 2009). In this study, we apply the tesseral method to compute the aforementioned gravity-gradient contributions. This method is briefly described below.

The radial gravity-gradient data were calculated using the following generalized formula (Grombein et al., 2013)

$$\delta T_{rr}^p(r, \phi, \lambda) = G\Delta\rho \int_{\lambda_1}^{\lambda_2} \int_{\phi_1}^{\phi_2} \int_{r_1}^{r_2} I_{rr}(r', \phi', \lambda') dr' d\phi' d\lambda', \quad (2)$$

with the integral kernel given by

$$I_{rr}(r', \phi', \lambda') = \left(\frac{3\Delta_r \Delta_r}{l^5} - \frac{1}{l^3} \right) K, \quad (3)$$

where $G = 6.674 \times 10^{-11} \text{ m}^3 \text{ kg}^{-1} \text{ s}^{-2}$ is Newton's gravitational constant and $\Delta\rho = \rho - \rho_c$ is the density contrast with respect to the reference crustal density. The index $p = t, b, s, c$ defines a particular type of the gravity-gradient correction (topographic, bathymetric, sediment, and consolidated crust). We further define the following parameters:

$$\Delta_r = r' \cos\psi - r, \quad (4)$$

$$l = \sqrt{r'^2 + r^2 - 2r'r \cos\psi}, \quad (5)$$

$$\cos\psi = \sin\phi \sin\phi' + \cos\phi \cos\phi' \cos(\lambda' - \lambda), \quad (6)$$

$$\kappa = r'^2 \cos\phi'. \quad (7)$$

The 3-D position is defined by the radius r , spherical latitude ϕ and longitude λ .

The integral function in Eq. (2) can be solved using the Gauss-Legendre quadrature rule (Asgharzadeh et al., 2007; Wild-Pfeiffer, 2008). Hence

$$\delta T_{rr}^p(r, \phi, \lambda) \approx G\Delta\rho \frac{(\lambda_2 - \lambda_1)(\phi_2 - \phi_1)(r_2 - r_1)}{8} \sum_{k=1}^{N^{\lambda}} \sum_{j=1}^{N^{\phi}} \sum_{i=1}^{N^r} W_i^r W_j^{\phi} W_k^{\lambda} I_{rr}(r'_i, \phi'_j, \lambda'_k), \quad (8)$$

where W_i^r, W_j^{ϕ} and W_k^{λ} are weighting coefficients, and N^r, N^{ϕ} and N^{λ} are the numbers of quadrature nodes (i.e., the order of the quadrature), for the radius, latitude and longitude, respectively. In our numerical study we used the third order of the quadrature.

2.2. Moho recovery

The gravitational potential generated by the Moho geometry can be

defined by

$$\delta V^m(r, \Omega) = G \iint_{\Omega' \in \Phi} \Delta\rho^{c/m}(\Omega') \int_{r'=R-D_0(\Omega')}^{R-D} l^{-1}(r, \psi, r') r'^2 dr' d\Omega', \quad (9)$$

where $R = 6371 \times 10^3 \text{ m}$ is the Earth's mean radius, $\Delta\rho^{c/m}$ is the laterally varying Moho density contrast, l is the Euclidean spatial distance, ψ is the spherical angle, $d\Omega' = \cos\phi' d\phi' d\lambda'$ is the infinitesimal surface element and Φ is a full spatial angle. The geocentric radius r of the observation surface point is computed as $r = R + H$, where H is the computational height. The Moho depth D is taken relative to the geoid surface (approximated by R), and D_0 is the mean Moho depth.

The spectral representation of l^{-1} for the external convergence domain $r \geq r'$ reads (e.g., Heiskanen and Moritz, 1967, p. 33, Eqs. 1–81)

$$l^{-1} = \frac{1}{r} \sum_{n=0}^{\infty} \left(\frac{r'}{r} \right)^n P_n(t), \quad (10)$$

where P_n is the Legendre polynomial of degree n and the argument $t = \cos\psi$.

According to Eq. (9), the gravitational gradient generated by the Moho geometry reads

$$\delta \Gamma_{rr}^m(r, \Omega) = \frac{\partial^2 \delta V^m(r, \Omega)}{\partial r^2} = G \iint_{\Omega' \in \Phi} \Delta\rho^{c/m}(\Omega') \int_{r'=R-D_0(\Omega')}^{R-D} \frac{\partial^2 l^{-1}(r, \psi, r')}{\partial r^2} r'^2 dr' d\Omega'. \quad (11)$$

From Eq. (10), the second-order radial derivative of l^{-1} in Eq. (11) is given by

$$\begin{aligned} \frac{\partial^2 l^{-1}(r, \psi, r')}{\partial r^2} &= \frac{1}{r'^2} \sum_{n=0}^{\infty} (r')^{n+2} (n+1)(n+2) \frac{1}{r^{n+3}} P_n(t) \\ &= \sum_{n=0}^{\infty} \frac{r'^n}{r^{n+3}} (n+1)(n+2) P_n(t). \end{aligned} \quad (12)$$

Inserting Eq. (12) into Eq. (11) it becomes

$$\delta \Gamma_{rr}^m(r, \Omega) = G \iint_{\Omega' \in \Phi} \Delta\rho^{c/m}(\Omega') \int_{r'=R-D_0(\Omega')}^{R-D} \sum_{n=0}^{\infty} \frac{r'^n}{r^{n+3}} (n+1)(n+2) P_n(t) r'^2 dr' d\Omega'. \quad (13)$$

We further define

$$\delta \Gamma_{rr}^m(r, \Omega) = G \iint_{\Omega' \in \Phi} \Delta\rho^{c/m}(\Omega') K(r, t, D) d\Omega', \quad (14)$$

where the radial integral kernel on the right-hand side of Eq. (14) is found to be

$$\begin{aligned} K(r, t, D) &= \int_{r'=R-D_0(\Omega')}^{R-D} \sum_{n=0}^{\infty} \frac{r'^{n+2}}{r^{n+3}} (n+1)(n+2) P_n(t) dr' \\ &= \sum_{n=0}^{\infty} \frac{(n+1)(n+2)}{r^{n+3}} P_n(t) \int_{r'=R-D_0(\Omega')}^{R-D} r'^{n+2} dr' \\ &= \sum_{n=0}^{\infty} \frac{(n+1)(n+2)}{r^{n+3}} P_n(t) \frac{1}{n+3} [(R-D)^{n+3} - (R-D_0)^{n+3}] \\ &= - \sum_{n=0}^{\infty} \frac{(n+1)(n+2)}{r^{n+3}} P_n(t) \frac{1}{n+3} \left[1 - \left(\frac{R-D}{R-D_0} \right)^{n+3} \right] (R-D_0)^{n+3} \\ &= - \sum_{n=0}^{\infty} \frac{(n+1)(n+2)}{(n+3)} \left(\frac{R-D_0}{r} \right)^{n+3} \left[1 - \left(\frac{R-D}{R-D_0} \right)^{n+3} \right] P_n(t) \end{aligned} \quad (15)$$

The expression in Eq. (14) is a non-linear Fredholm integral equation of the first kind (e.g., Sjöberg, 2009). Its linearization is done by applying a Taylor series with respect to the mean Moho depth D_0 , while disregarding higher than the first-order terms. Hence

$$K(r, t, D) \approx K(r, t, D_0) + \frac{\partial}{\partial D} K(r, t, D)|_{D=D_0} (D - D_0). \quad (16)$$

For $D = D_0$, we have $K(r, t, D_0) = 0$. Consequently, we arrive at

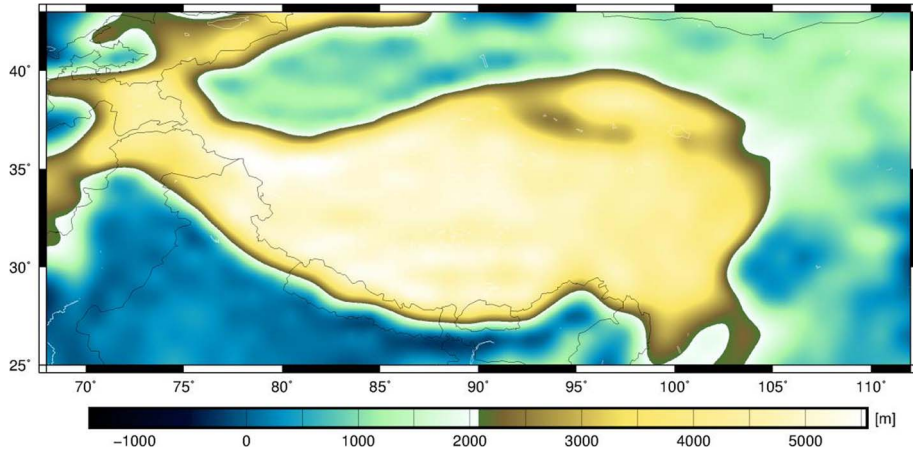


Fig. 1. The topography and bathymetry of the study area.

$$\delta\Gamma_{rr}^m(r, \Omega) \cong G \iint_{\Omega' \in \Phi} \Delta\rho^{c/m}(\Omega') \frac{\partial}{\partial D} K(r, t, D)|_{D=D_0} dD' d\Omega', \quad (17)$$

where

$$\begin{aligned} W(r, t, D_0) &= \frac{\partial}{\partial D} K(r, t, D)|_{D=D_0} \\ &= - \sum_{n=0}^{\infty} \frac{(n+1)(n+2)}{n+3} \left(\frac{R-D_0}{r} \right)^{n+3} \left[-(n+3) \left(\frac{R-D}{R-D_0} \right)^{n+2} \frac{-1}{R-D_0} \right] P_n(t)|_{D=D_0} \\ &= - \sum_{n=0}^{\infty} \frac{(n+1)(n+2)}{n+3} \left(\frac{R-D_0}{r} \right)^{n+3} P_n(t) \frac{(n+3)}{R-D_0} \left(\frac{R-D}{R-D_0} \right)^{n+2} |_{D=D_0} \\ &= - \sum_{n=0}^{\infty} (n+2)(n+1) \frac{(R-D)^{n+2}}{r^{n+3}} P_n(t)|_{D=D_0} \\ &= - \frac{1}{R-D_0} \sum_{n=0}^{\infty} (n+2)(n+1) \left(\frac{R-D_0}{r} \right)^{n+3} P_n(t) \end{aligned} \quad (18)$$

Denoting $\tau = (R-D_0)/r$, then the spectral representation of $W(t, \tau)$ in Eq. (18) becomes

$$\begin{aligned} W(t, \tau) &= - \frac{1}{R-D_0} \sum_{n=0}^{\infty} \tau^{n+3} (n+1)(n+2) P_n(t) \\ &= - \frac{\tau^3}{R-D_0} \sum_{n=0}^{\infty} \tau^n (n^2 + 3n + 2) P_n(t) \\ &= - \frac{\tau^3}{R-D_0} \left[2 + \sum_{n=1}^{\infty} \tau^n n^2 P_n(t) + 3 \sum_{n=1}^{\infty} \tau^n n P_n(t) + 2 \sum_{n=1}^{\infty} \tau^n P_n(t) \right] \end{aligned} \quad (19)$$

Furthermore, the closed-form formula of $W(t, \tau)$ is found to be (see Appendix A)

$$\begin{aligned} W(t, \tau) &= - \frac{\tau^3}{R-D_0} \left[2 + \frac{\tau^2[-Q+3(\tau-t)^2]-Q^2\tau(\tau-t)}{Q^5} + 3(-\frac{\tau(\tau-t)}{Q^3}) + 2(\frac{1}{Q}-1) \right] \\ &= - \frac{\tau^3}{R-D_0} \frac{2Q^4-5\tau^2Q^2+3\tau^2(\tau-t)^2+4Q^2\pi t}{Q^5} \end{aligned} \quad (20)$$

Finally, we arrive at

$$\delta\Gamma_{rr}^m(r, \Omega) \cong G \iint_{\Omega' \in \Phi} \Delta\rho^{c/m}(\Omega') W(t, \tau) dD' d\Omega'. \quad (21)$$

The integral in Eq. (21) can be discretized and solved numerically. Using the vector-matrix notation, the system of observation equations for finding the Moho depth corrections dD' is written as following

$$Ax = b + \epsilon, \quad (22)$$

where A denotes the design matrix (obtained by a discretization of the

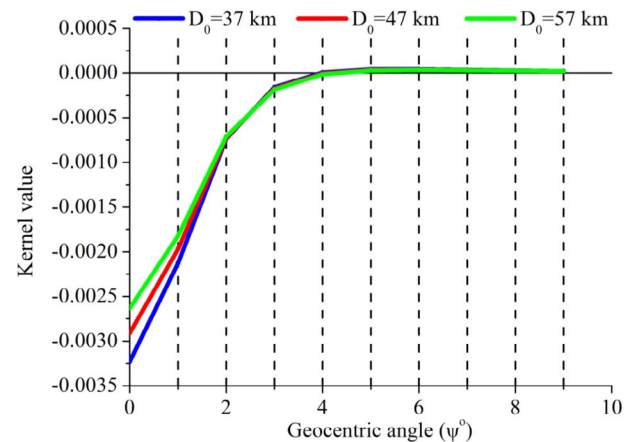
Fig. 2. The kernel behavior of $W(\psi)$.

Table 1
Statistics of the gravity-gradient contributions.

Gravity-gradient component	Min [E]	Max [E]	Mean [E]	STD [E]
δT_{rr}^t	-1.38	-6.75	-1.77	2.23
δT_{rr}^b	0.20	0.71	0.12	0.13
δT_{rr}^s	0.92	0.25	0.05	0.24
δT_{rr}^c	-2.54	-0.24	-1.36	0.48

Table 2

Statistics of the (step-wise) corrected gravity gradients: the GOCO05S gravity-gradient δT_{rr} , the topography-corrected gravity-gradient δT_{rr}^T , the topography and bathymetry-corrected gravity-gradient δT_{rr}^{TB} , the topography corrected, bathymetry and sediment-corrected gravity-gradient δT_{rr}^{TBS} , and the consolidated crust-stripped gravity-gradient δT_{rr}^{CS} .

Gravity-gradient data	Min [E]	Max [E]	Mean [E]	STD [E]
δT_{rr}	-1.47	1.21	-0.03	0.42
δT_{rr}^T	-6.10	1.00	-1.80	1.97
δT_{rr}^{TB}	-6.15	0.66	-1.93	1.93
δT_{rr}^{TBS}	-6.31	1.32	-1.88	2.04
δT_{rr}^{CS}	-8.76	1.08	-3.24	2.41

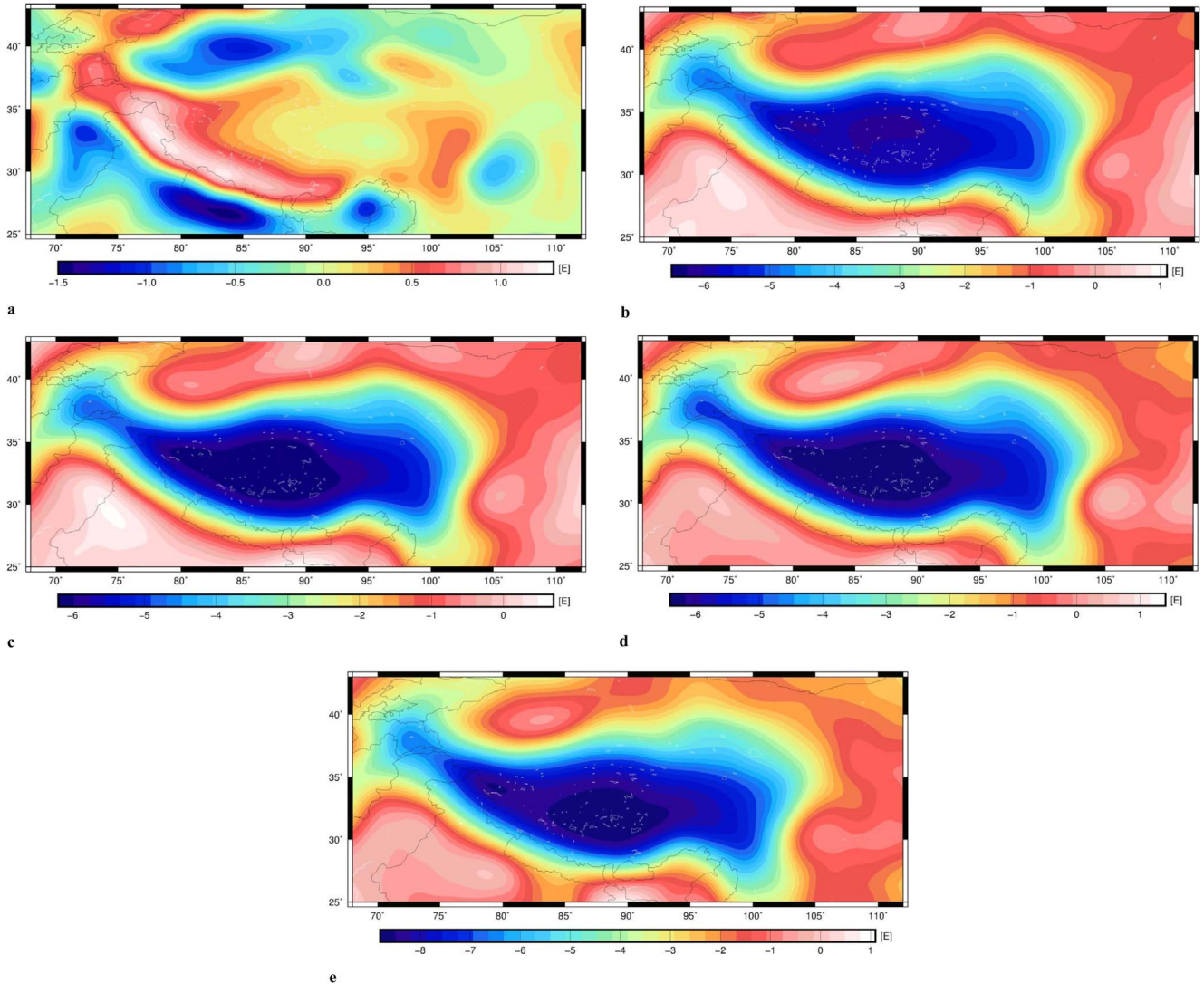


Fig. 3. The step-wise corrected gravity-gradient data: (a) the GOCO05S gravity-gradient, (b) the topography-corrected gravity-gradient, (c) the topography and bathymetry-corrected gravity-gradient, (d) the topography, bathymetry and sediment-corrected gravity-gradient, and (e) the consolidated crust-stripped gravity-gradient.

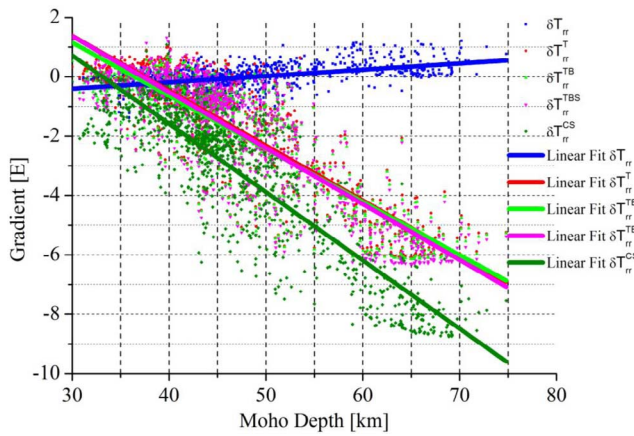


Fig. 4. Spatial correlation between the gravity-gradient data and the CRUST1.0 Moho depth.

integral in Eq. (21)), \mathbf{x} denotes the vector of the unknown Moho depth corrections with respect to the mean Moho depth, \mathbf{b} is the vector of observations (computed according to Eq. (1)), and ϵ is the vector of residuals.

Since the system of observation equations in Eq. (22) is generally ill-

conditioned, its inverse solution is sensitive to the observation data noise. To stabilize the solution, we applied the Tikhonov regularization (Phillips, 1962; Tikhonov, 1963; Tikhonov and Arsenin, 1977) by minimizing the following weighted combination of the residual norm and the side constraint

$$\min \{ \| \mathbf{Ax} - \mathbf{b} \|_2^2 + \alpha^2 \| \mathbf{x} \|_2^2 \}, \quad (23)$$

where α is the regularization parameter. A good choice of the regularization parameter should yield a fair balance between the perturbation error and the regularization error in the regularized solution. To find the optimal regularization parameter we applied the Generalized Cross-Validation (GCV) technique.

Combining Eqs. (22) and (23), the solution for \mathbf{x} is obtained from

$$\mathbf{x}_{reg} = (\mathbf{A}^T \mathbf{A} + \alpha^2 \mathbf{I})^{-1} \mathbf{A}^T \mathbf{b}, \quad (24)$$

where \mathbf{x}_{reg} is the regularized solution which generally reduces a propagation of the noise in input data into the result.

3. Numerical realization and discussion

The numerical procedures described in Section 2 were applied to recover the Moho depth under Tibet. The results and discussion are presented next.

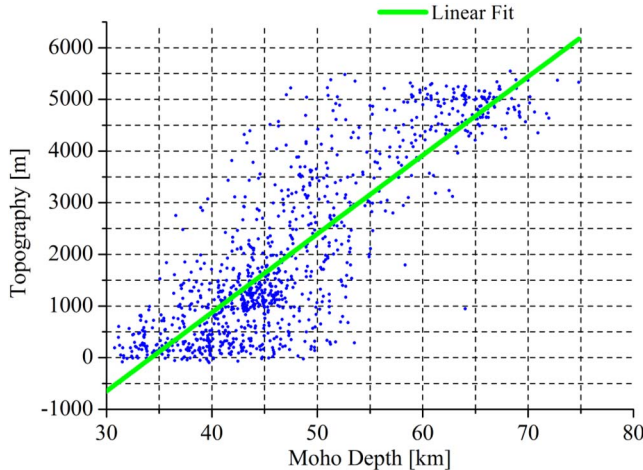


Fig. 5. Spatial correlation between the Moho depth and topography.

3.1. Data acquisition

The regional study area of Tibet is bounded by the parallels of 23.5 and 44.5 arc-deg northern latitudes and the meridians of 64.5 and 114.5 arc-deg eastern longitudes. Fig. 1 shows the topography and bathymetry of the study area. As for the geographical and tectonic names under the study area, we refer readers to e.g., Shin et al. (2015). The topography and bathymetry were generated from the 1×1 arc-min ETOPO1 data (Amante and Eakins, 2009) by applying a spatial averaging onto 1×1 arc-deg grid. The solution of Eq. (24) should be optimally carried out by using global data coverage. However, in regional applications, the inversion can be performed using only regional datasets, under the assumption that the contribution from a distant zone (i.e., truncation error) is negligible (e.g., Eshagh, 2011; Bagherbandi and Eshagh, 2012a, 2012b). Based on the kernel behavior shown in Fig. 2, we can see that the truncation error is reduced significantly from distant zone beyond 4 arc-deg (e.g., Eshagh, 2014).

The disturbing gravity gradients δT_r were computed from the GOCO05S coefficients (Mayer-Gürr et al., 2015) up to the spherical harmonic degree of 180. The normal gravity-gradient component was evaluated according to the GRS80 (Moritz, 2000) parameters. Then we applied the tesseroid method to calculate the gravity-gradient corrections. The topographic and bathymetric gravity-gradient contributions were computed from the ETOPO1 data. The average density of upper continent crust of 2670 kg m^{-3} (Hinze, 2003) was used as the topographic density. The same density value was adopted in definition of the reference crustal density. The bathymetric density contrast was

Table 3
Statistics of the CRUST1.0 Moho density contrast.

CRUST1.0 Moho density contrast	Min [kg m^{-3}]	Max [kg m^{-3}]	Mean [kg m^{-3}]	STD [kg m^{-3}]
Upper mantle – reference crust	560	780	688	40
Upper mantle – lower crust	250	600	448	70

defined according to the seawater density-depth equation (Tenzer et al., 2010, 2011, 2012a, 2012d; Gladkikh and Tenzer, 2012). The gravity-gradient contributions for the sediments and consolidated crust were computed from the CRUST1.0 data. In order to remove the long-wavelength gravitational spectrum, the harmonic coefficients up to degree 17 were subtracted (cf. Bagherbandi and Sjöberg, 2012). All computations were realized at the GOCE mean satellite elevation of 255 km.

Statistics of the gravity-gradient corrections and the (step-wise) corrected gravity gradients are summarized in Tables 1 and 2. The intermediate results (step-wise) of computing the refined gravity gradients δT_{rr}^{cs} (cf. Eq. (1)) are shown in Fig. 3. We further investigated a spatial correlation between the gravity gradients and the CRUST1.0 Moho depth. As can be seen in Fig. 4, the refined gravity-gradient data have a maximum (absolute) correlation with the Moho geometry. In addition, we plotted the spatial correlation between the topographic heights and the CRUST1.0 Moho depth (see Fig. 5). We could see a clear spatial correlation between the Moho depth and the topography, which is a basic principle utilized in the Airy-Heiskanen (e.g. Heiskanen and Moritz, 1967, p. 135) isostatic model. However, large discrepancies with respect to a linear trend could not be realistically modeled by applying this simple isostatic principle.

3.2. Choice of the Moho density contrast

The choice of the variable Moho density contrast is essential for a global gravimetric Moho recovery (cf. Tenzer et al., 2015b). In regional studies, the choice of the uniform Moho density contrast might be sufficient, especially when the expected uncertainties of the Moho density contrast are at the same level or even larger than values of the estimated Moho density contrast.

Various values of the Moho density contrast were reported in the existing studies. For instance, Tenzer et al. (2015a) estimated that the global average value of the Moho density contrast equals to 445 kg m^{-3} based on the analysis of CRUST1.0 data. Sjöberg and Bagherbandi (2011) reported the value of 448 kg m^{-3} , which closely agrees with the value estimated by Tenzer et al. (2015a), but differs about 7% from

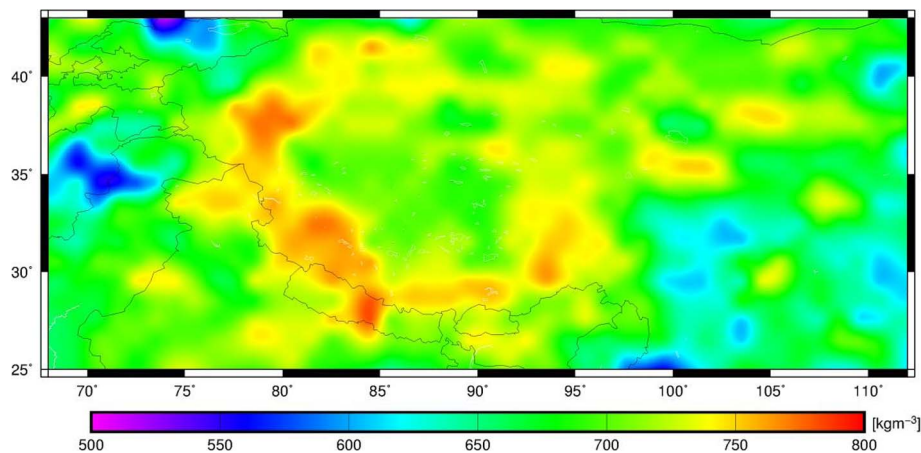


Fig. 6. Moho density contrast with respect to the reference crustal density of 2670 kg m^{-3} .

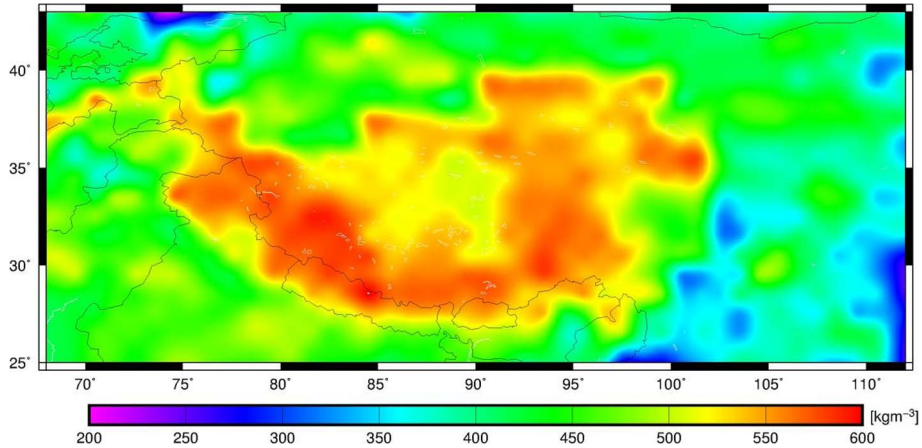


Fig. 7. CRUST1.0 Moho density contrast.

Table 4

Statistics of the Moho solutions: $D_{CRUST1.0}$ – the CRUST1.0 seismic model, $D_{uniform}$ – the gravimetric Moho model (for the uniform Moho density contrast), $D_{um-2670}$ – the gravimetric Moho model (for the variable Moho density contrast with respect to the reference crustal density), and D_{um-lc} – the gravimetric Moho model (for the CRUST1.0 Moho density contrast).

Moho depth	Min [km]	Max [km]	Mean [km]	STD [km]
$D_{CRUST1.0}$	30.0	74.8	47.2	9.2
$D_{uniform}$	29.3	71.7	46.5	9.2
$D_{um-2670}$	29.0	70.5	48.2	7.8
D_{um-lc}	25.9	74.2	48.4	8.5

both the value of 485 kg m^{-3} estimated from the analysis of CRUST2.0 data by Tenzer et al. (2012b) and the value of 480 kg m^{-3} reported in PREM (cf. Dziewonski and Anderson, 1981). Sjöberg and Bagherbandi (2011) also provided the average Moho density contrast of $678 \pm 78 \text{ kg m}^{-3}$ for the continental crust with maxima of 998 kg m^{-3} under Tibet. Burov et al. (1990) adopted the Moho density contrast of 600 kg m^{-3} under Tian Shan. Eshagh et al. (2016) estimated that the Moho density contrast value in central Eurasia is typically larger than 450 kg m^{-3} . In this study, we applied the estimation principle proposed by Tenzer et al. (2015a). According to our result, the average value of the Moho density contrast at the study area equals to 602 kg m^{-3} .

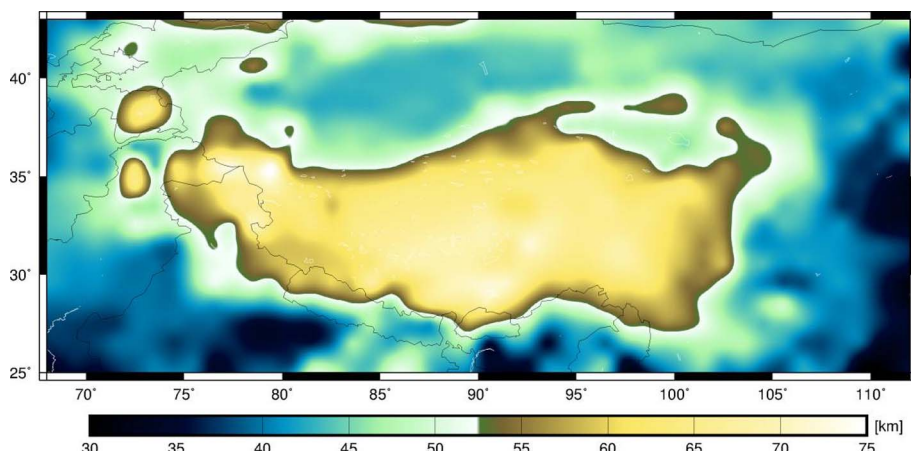
We further used the CRUST1.0 upper mantle data to define the variable Moho density contrast (with respect to the reference crustal density of 2670 kg m^{-3}). The result is shown in Fig. 6, with the

statistical summary given in Table 3. The Moho density contrast varies from 560 kg m^{-3} to 780 kg m^{-3} . We note that the mean value of 688 kg m^{-3} (cf. Table 3) differs from our estimate value of 602 kg m^{-3} . The variable Moho density contrast with respect to the reference crustal density obviously does not correspond to the real density contrast at the Moho interface. To illustrate the variable Moho density contrast, we used the CRUST1.0 lower crust and upper mantle density data (see Fig. 7). In this case, the Moho density contrast varies from 250 kg m^{-3} to 600 kg m^{-3} , with a mean value of 448 kg m^{-3} .

3.3. Moho results and discussion

The refined gravity-gradient data were used to determine the Moho depth at the study area of Tibet. We determined the Moho depth for the uniform and variable Moho density contrast models. Prior to solving the gravimetric Moho inversion, the mean Moho depth was chosen so that it closely represented the Moho geometry of a particular study area. For this purpose, we used the CRUST1.0 mean Moho depth value of 47.2 km (cf. Table 4). The results of gravimetric Moho inversion for the uniform and variable Moho density contrast, including the CRUST1.0 Moho density contrast, are presented in Figs. 8–10, with the statistical summary given in Table 4. As can be seen in Fig. 8, the maximum Moho depth under Tibet reaches to 70 km . The Moho under the Tarim basin is typically about 50 km , while deepens to about $55\text{--}65 \text{ km}$ under the Qaidam basin. The Moho depth under the Sichuan basin gradually decreases to about 45 km , and reaches the regional minimal of about 35 km in the southeast China.

Despite overall similarities between these three gravimetric Moho

Fig. 8. Moho depth solution $D_{uniform}$ (for the uniform Moho density contrast).

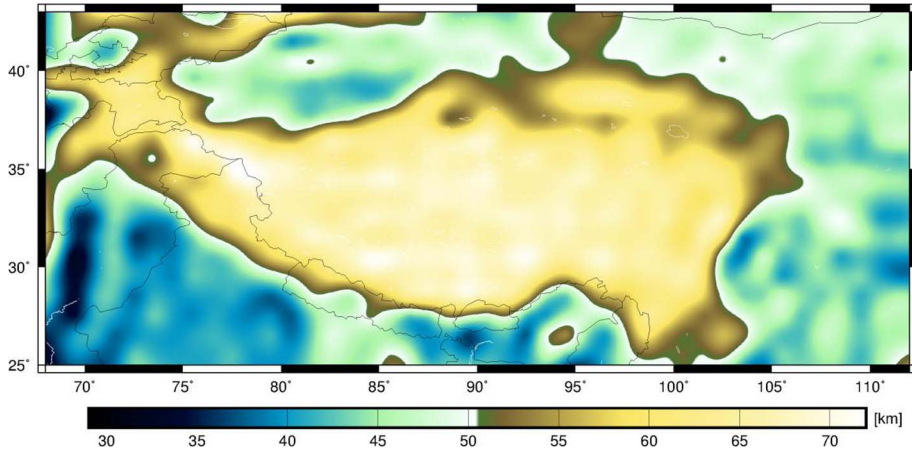


Fig. 9. Moho depth solution $D_{um-2670}$ (for the variable Moho density contrast with respect to the reference crustal density).

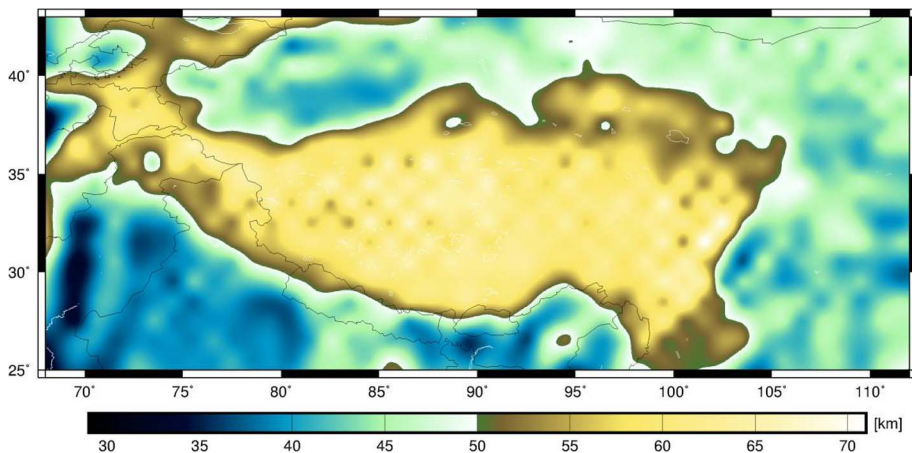


Fig. 10. Moho depth solution D_{um-lc} (for the CRUST1.0 Moho density contrast).

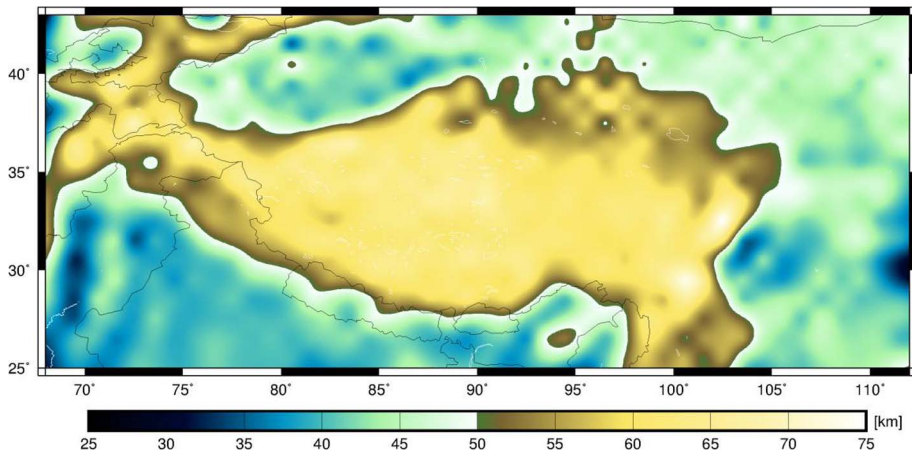


Fig. 11. CRUST1.0 Moho model $D_{CRUST1.0}$.

depth solutions, some localized differences attributed to the Moho density contrast variations are seen in the central Tibet, Qaidam basin and the western part of Sichuan basin.

The gravimetric Moho solutions (Figs. 8–10) were compared with the CRUST1.0 Moho model (Fig. 11). The Moho depth differences are shown in Fig. 12, with the statistical summary given in Table 5. Surprisingly, the best RMS fit with CRUST1.0 (4.9 km) is attained when using the uniform Moho density contrast. We explain this by a low accuracy of the CRUST1.0 lower crust and upper mantle data in this part of the world, which is also confirmed by the fact that the average

value of the CRUST1.0 Moho density contrast of 688 kg m^{-3} (cf. Table 3) differs significantly from our estimated value of 602 kg m^{-3} .

4. Conclusions

We developed a novel algorithm for a regional Moho recovery in spatial domain from the gravity-gradient data and applied it for Tibet. This algorithm facilitates the gravimetric forward modeling based on using the tesseral method to model the gravitational contributions of crustal density heterogeneities. Moreover, the spectral filtering techni-

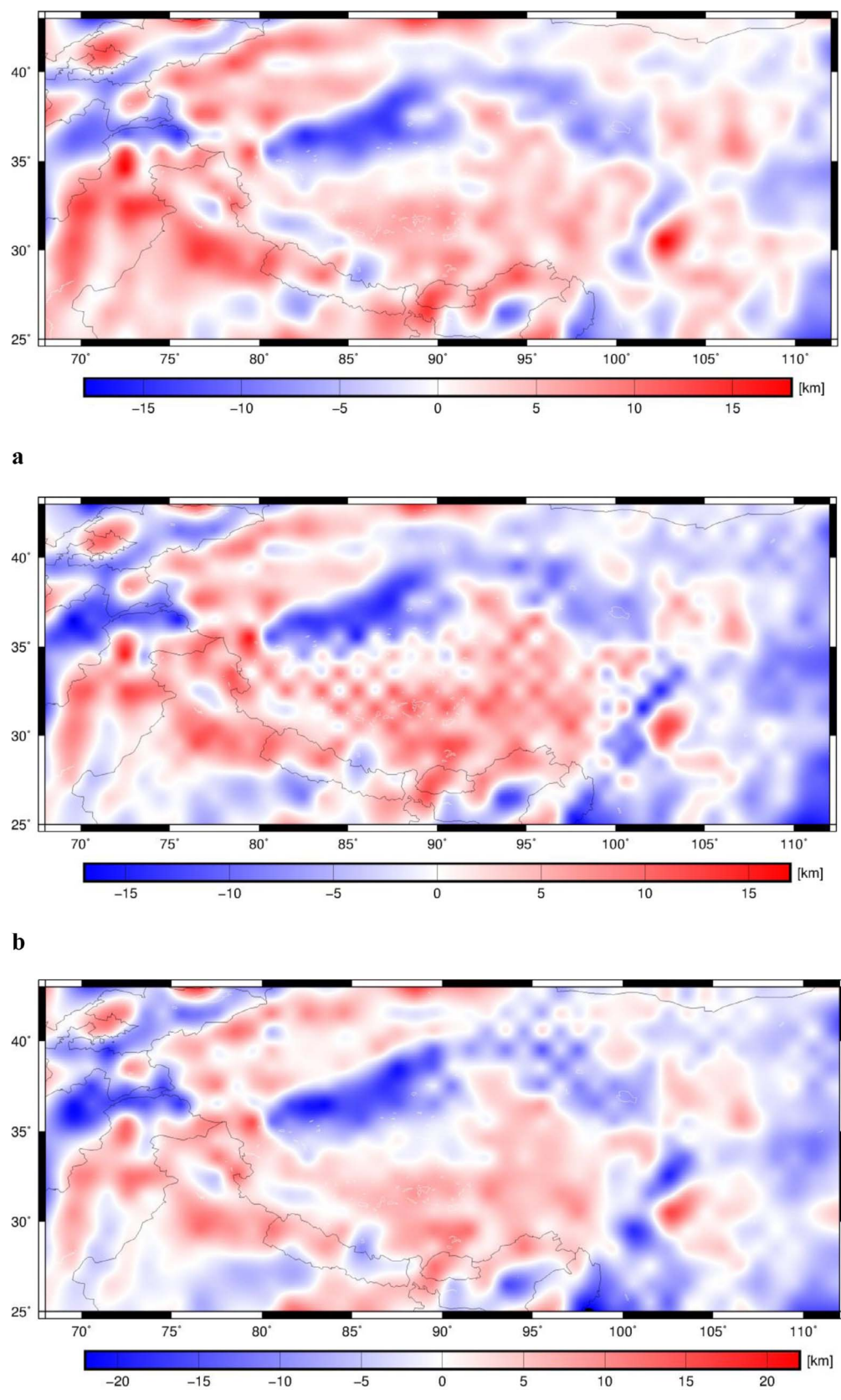


Fig. 12. Moho depth differences: (a) $D_{\text{Crust1.0}} - D_{\text{uniform}}$, (b) $D_{\text{Crust1.0}} - D_{\text{um-2670}}$, and (c) $D_{\text{Crust1.0}} - D_{\text{um-lc}}$.

Table 5
Statistics of the Moho depth differences.

Moho depth difference	Min [km]	Max [km]	Mean [km]	RMS [km]
$D_{CRUST1.0} - D_{uniform}$	-14.7	17.3	0.7	4.9
$D_{CRUST1.0} - D_{um2670}$	-16.7	15.4	-1.0	5.7
$D_{CRUST1.0} - D_{um-lc}$	-21.1	15.2	-1.2	5.4

que is applied to remove the long-wavelength signature of the mantle density heterogeneities. The regional gravimetric Moho inversion was carried out by solving the system of observation equations, which was obtained based on the linearization and further discretization of the (nonlinear) Fredholm integral equation of the first kind. A selection of the data-area extension was done empirically by checking a spatial behavior of the integral kernel, which functionally related the Moho depth with the gravity-gradient data. In our case, the data-area

Appendix A. Closed-form formula of the integral kernel $W(t, \tau)$

In view of Eq. (10) we thus obtain the following identity

$$\sum_{n=0}^{\infty} \tau^n P_n(t) = \frac{1}{\sqrt{1 + \tau^2 - 2\tau t}} = \frac{1}{Q}. \quad (\text{A.1})$$

The first- and second-order derivatives of Eq. (A.1) with respect to τ are found to be

$$\begin{aligned} \sum_{n=0}^{\infty} n\tau^{n-1} P_n(t) &= -\frac{1}{2}(1 + \tau^2 - 2\tau t)^{-\frac{3}{2}}(2\tau - 2t) \\ &= -(\tau - t)(1 + \tau^2 - 2\tau t)^{-\frac{3}{2}} \end{aligned} \quad (\text{A.2})$$

and

$$\begin{aligned} \sum_{n=0}^{\infty} n(n-1)\tau^{n-2} P_n(t) &= -[(1 + \tau^2 - 2\tau t)^{-\frac{3}{2}} + (\tau - t)(-\frac{3}{2})(1 + \tau^2 - 2\tau t)^{-\frac{5}{2}}(2\tau - 2t)] \\ &= -(1 + \tau^2 - 2\tau t)^{-\frac{3}{2}} + 3(\tau - t)^2(1 + \tau^2 - 2\tau t)^{-\frac{5}{2}} \\ &= \frac{[-(1 + \tau^2 - 2\tau t) + 3(\tau - t)^2]}{(1 + \tau^2 - 2\tau t)^{\frac{5}{2}}} \end{aligned} \quad (\text{A.3})$$

We further separate the left-hand side of Eq. (A.3) into two parts, hence

$$\tau^{-2} \sum_{n=0}^{\infty} \tau^n n^2 P_n(t) - \tau^{-2} \sum_{n=0}^{\infty} \tau^n n P_n(t) = \frac{[-(1 + \tau^2 - 2\tau t) + 3(\tau - t)^2]}{(1 + \tau^2 - 2\tau t)^{\frac{5}{2}}}, \quad (\text{A.4})$$

With simple mathematical work, Eq. (A.4) becomes

$$\sum_{n=0}^{\infty} \tau^n n^2 P_n(t) = \frac{\tau^2[-(1 + \tau^2 - 2\tau t) + 3(\tau - t)^2]}{(1 + \tau^2 - 2\tau t)^{\frac{5}{2}}} + \sum_{n=0}^{\infty} \tau^n n P_n(t). \quad (\text{A.5})$$

Inserting Eq. (A.2) into Eq. (A.5), we obtain

$$\begin{aligned} \sum_{n=0}^{\infty} \tau^n n^2 P_n(t) &= \frac{\tau^2[-(1 + \tau^2 - 2\tau t) + 3(\tau - t)^2]}{(1 + \tau^2 - 2\tau t)^{\frac{5}{2}}} + \frac{-\tau(\tau - t)}{Q^3} \\ &= \frac{\tau^2[-Q^2 + 3(\tau - t)^2] - Q^2\tau(\tau - t)}{Q^5} \end{aligned} \quad (\text{A.6})$$

According to Eqs.(A.1), (A.2) and (A.6), we get the following identities:

$$\sum_{n=1}^{\infty} \tau^n P_n(t) = \frac{1}{Q} - 1, \quad (\text{A.7})$$

$$\sum_{n=1}^{\infty} n\tau^n P_n(t) = -\frac{\tau(\tau - t)}{Q^3}, \quad (\text{A.8})$$

$$\sum_{n=1}^{\infty} n^2 \tau^n P_n(t) = \frac{\tau^2[-Q^2 + 3(\tau - t)^2] - Q^2\tau(\tau - t)}{Q^5}, \quad (\text{A.9})$$

Substituting Eqs. (A.7)–(A.9) into Eq. (19), then the resulting closed-form formula of the integral kernel $W(t, \tau)$ is found to be

$$\begin{aligned}
 W(t, \tau) &= -\frac{\tau^3}{R-D_0} \left[2 + \frac{\tau^2[-Q+3(\tau-t)^2]-Q^2\tau(\tau-t)}{Q^5} + 3\left(-\frac{\tau(\tau-t)}{Q^3}\right) + 2\left(\frac{1}{Q}-1\right) \right] \\
 &= -\frac{\tau^3}{R-D_0} \frac{2Q^4-5\tau^2Q^2+3\tau^2(\tau-t)^2+4Q^2t\tau}{Q^5}
 \end{aligned} \tag{A.10}$$

References

- Amante, C., Eakins, B.W., 2009. ETOPO1 1 arc-minute global relief model: procedures, data sources and analysis (p. 19). Colorado: US Department of Commerce, National Oceanic and Atmospheric Administration, National Environmental Satellite, Data, and Information Service, National Geophysical Data Center, Marine Geology and Geophysics Division.
- Asgharzadeh, M.F., Von Frese, R.R.B., Kim, H.R., Leftwich, T.E., Kim, J.W., 2007. Spherical prism gravity effects by Gauss-Legendre quadrature integration. *Geophys. J. Int.* 169 (1), 1–11.
- Bagdassarov, N., Batalev, V., Egorova, V., 2011. State of lithosphere beneath Tien Shan from petrology and electrical conductivity of xenoliths. *J. Geophys. Res.: Solid Earth* 116 (B1).
- Bagherbandi, M., Sjöberg, L.E., 2012. Non-isostatic effects on crustal thickness: a study using CRUST2.0 in Fennoscandia. *Phys. Earth Planet. Inter.* 200, 37–44. <http://dx.doi.org/10.1016/j.pepi.2012.04.001>.
- Bagherbandi, M., 2012. A comparison of three gravity inversion methods for crustal thickness modelling in Tibet plateau. *J. Asian Earth Sci.* 43 (1), 89–97. <http://dx.doi.org/10.1016/j.jseaes.2011.08.013>.
- Bagherbandi, M., Eshagh, M., 2012a. Crustal thickness recovery using an isostatic model and GOCE data. *Earth, Planets and Space* 64 (11), 1053–1057. <http://dx.doi.org/10.5047/eps.2012.04.009>.
- Bagherbandi, M., Eshagh, M., 2012b. Recovery of Moho's undulations based on the Vening Meinesz-Moritz theory from satellite gravity gradiometry data: a simulation study. *Adv. Space Res.* 49 (6), 1097–1111. <http://dx.doi.org/10.1016/j.asr.2011.12.033>.
- Bump, H.A., Sheehan, A.F., 1998. Crustal thickness variations across the northern Tien Shan from teleseismic receiver functions. *Geophys. Res. Lett.* 25 (7), 1055–1058.
- Burov, E.V., Kogan, M.G., Lyon-Caen, H., Molnar, P., 1990. Gravity anomalies, the deep structure, and dynamic processes beneath the Tien Shan. *Earth Planet. Sci. Lett.* 96 (3), 367–383.
- Dziewonski, A.M., Anderson, D.L., 1981. Preliminary reference Earth model. *Phys. Earth Planet. Inter.* 25 (4), 297–356.
- Eckhardt, D.H., 1983. The gains of small circular, square and rectangular filters for surface waves on a sphere. *Bullet. Géodésique* 57 (1–4), 394–409. <http://dx.doi.org/10.1007/BF02502094>.
- Eshagh, M., Bagherbandi, M., Sjöberg, L., 2011. A combined global Moho model based on seismic and gravimetric data. *Acta Geodaetica et Geophysica Hungarica* 46 (1), 25–38. <http://dx.doi.org/10.1556/AGeo.46.2011.1.3>.
- Eshagh, M., 2011. The effect of spatial truncation error on integral inversion of satellite gravity gradiometry data. *Adv. Space Res.* 47 (7), 1238–1247.
- Eshagh, M., 2014. Determination of Moho discontinuity from satellite gradiometry data: linear approach. *Geodyn. Res. Int. Bullet.* 1 (2), 1–13.
- Eshagh, M., Hussain, M., Tenzer, R., Romeshkani, M., 2016. Moho density contrast in central Eurasia from GOCE gravity gradients. *Remote Sens.* 8 (418), 1–18.
- Eshagh, M., Hussain, M., 2016. An approach to Moho discontinuity recovery from on-orbit GOCE data with application over Indo-Pak region. *Tectonophysics* 690, 253–262.
- Floerberghagen, R., Fehringer, M., Lamarre, D., Muzi, D., Frommknecht, B., Steiger, C., Da Costa, A., 2011. Mission design, operation and exploitation of the gravity field and steady-state ocean circulation explorer mission. *J. Geodesy* 85 (11), 749–758. <http://dx.doi.org/10.1007/s00190-011-0498-3>.
- Gao, R., Lu, Z., Li, Q., Guan, Y., Zhang, J., He, R., Huang, L., 2005. Geophysical survey and geodynamic study of crust and upper mantle in the Qinghai-Tibet Plateau. *Episodes* 28 (4), 263.
- Gladkikh, V., Tenzer, R., 2012. A mathematical model of the global ocean saltwater density distribution. *Pure Appl. Geophys.* 169 (1–2), 249–257. <http://dx.doi.org/10.1007/s00024-011-0275-5>.
- Gómez-Ortiz, D., Agarwal, B.N.P., Tejero, R., Ruiz, J., 2011. Crustal structure from gravity signatures in the Iberian Peninsula. *Geol. Soc. Am. Bull.* 123 (7–8), 1247–1257. <http://dx.doi.org/10.1130/B30224.1>.
- Grombein, T., Seitz, K., Heck, B., 2013. Optimized formulas for the gravitational field of a tesseract. *J. Geodesy*. <http://dx.doi.org/10.1007/s00190-013-0636-1>.
- Heiskanen, W.A., Moritz, H., 1967. Physical Geodesy. Freeman W.H., New York.
- Hinze, W.J., 2003. Bouguer reduction density, why 2.67? *Geophysics* 68 (5), 1559–1560. <http://dx.doi.org/10.1190/1.1620629>.
- Jin, Y., McNutt, M.K., Zhu, Y., 1994. Evidence from gravity and topography data for folding of Tibet. *Nature* 371 (6499), 669–674. <http://dx.doi.org/10.1038/371669a0>.
- Kind, R., Ni, J., Zhao, W., Wu, J., 1996. Evidence from earthquake data for a partially molten crustal layer in southern Tibet. *Science* 274 (5293), 1692.
- Kind, R., Yuan, X., Saul, J., Nelson, D., Sobolev, S.V., Mechie, J., Jiang, M., 2002. Seismic images of crust and upper mantle beneath Tibet: evidence for Eurasian plate subduction. *Science* 298 (5596), 1219–1221.
- Laske, G., Masters, G., Ma, Z., Pasyanos, M. (2013, April). Update on CRUST1.0-A 1-degree global model of Earth's crust. *Geophys. Res. Abstracts*, 15, 2658.
- Mayer-Gürr, T., et al., 2015. The Combined Satellite Gravity Field Model GOCO05s. Presentation at EGU 2015, Vienna, April 2015.
- Moritz, H., 1990. The inverse Vening Meinesz problem in isostasy. *Geophys. J. Int.* 102 (3), 733–738.
- Moritz, H., 2000. Geodetic reference system 1980. *J. Geodesy* 54 (3), 395–405.
- Nelson, K.D., Zhao, W., Brown, L.D., Kuo, J., Che, J., Liu, X., Kind, R., 1996. Partially molten middle crust beneath southern Tibet: synthesis of project INDEPTH results. *Science* 274 (5293), 1684–1688.
- Phillips, D.L., 1962. A technique for the numerical solution of certain integral equations of the first kind. *J. Assoc. Comput. Mach.* 9 (1), 84–97. <http://dx.doi.org/10.1145/321105.321114>.
- Roecker, S., 2001. Constraints on the crust and upper mantle of the Kyrgyz Tien Shan from the preliminary analysis of GHENGIS broad-band seismic data. *Russ. Geol. Geophys.* 42, 1554–1565.
- Rai, S.S., Priestley, K., Gaur, V.K., Mitra, S., Singh, M.P., Searle, M., 2006. Configuration of the Indian Moho beneath the NW Himalaya and Ladakh. *Geophys. Res. Lett.* 33 (15).
- Sampietro, D. (2011, March). GOCE Exploitation for MOHO MODELING and Applications. In: Proceedings of the 4th international GOCE user workshop, 31.
- Sampietro, D., Reguzzoni, M., Braatenberg, C., 2014. The GOCE estimated Moho beneath the Tibetan Plateau and Himalaya. In: *Earth on the Edge: Science for a Sustainable Planet*. Springer, Berlin Heidelberg, pp. 391–397.
- Sampietro, D., 2016. Crustal Modelling and Moho Estimation with GOCE Gravity Data. In: *Remote Sens. Adv. Earth Syst. Sci.* Springer International Publishing, pp. 127–144.
- Shin, Y.H., Choi, K.S., Xu, H., 2006. Three-dimensional forward and inverse models for gravity fields based on the Fast Fourier Transform. *Comput. Geosci.* 32 (6), 727–738. <http://dx.doi.org/10.1016/j.cageo.2005.10.002>.
- Shin, Y.H., Shum, C.K., Braatenberg, C., Lee, S.M., Na, S.H., Choi, K.S., Hsu, H., Park, Y.S., Lim, M., 2015. Moho topography, ranges and folds of Tibet by analysis of global gravity models and GOCE data. *Scientific Reports* 5.
- Sjöberg, L.E., 2009. Solving Vening Meinesz-Moritz inverse problem in isostasy. *Geophys. J. Int.* 179 (3), 1527–1536. <http://dx.doi.org/10.1111/j.1365-246X.2009.04397.x>.
- Sjöberg, L., Bagherbandi, M., 2011. A method of estimating the Moho density contrast with a tentative application of EGM08 and CRUST2.0. *Acta Geophys.* 59 (3), 502–525. <http://dx.doi.org/10.2478/s11600-011-0004-6>.
- Stauffer, P., 1993. Deep seismic reflection evidence for continental under thrusting beneath southern Tibet. *Nature* 366 (9).
- Tapley, B.D., Bettadpur, S., Watkins, M., Reigber, C., 2004a. The gravity recovery and climate experiment: mission overview and early results. *Geophys. Res. Lett.* 31 (9).
- Tapley, B.D., Bettadpur, S., Ries, J., Thompson, P.F., Watkins, M.M., 2004b. GRACE measurements of mass variability in the Earth system. *Science* 305 (5683), 503–505. <http://dx.doi.org/10.1126/science.1099192>.
- Tenzer, R., Chen, W., Tsoulis, D., Bagherbandi, M., Sjöberg, L.E., Novák, P., Jin, S., 2015a. Analysis of the refined CRUST1.0 crustal model and its gravity field. *Surv. Geophys.* 36 (1), 139–165.
- Tenzer, R., Chen, W., Jin, S., 2015b. Effect of the upper mantle density structure on the Moho geometry. *Pure Appl. Geophys.* 172 (6), 1563–1583. <http://dx.doi.org/10.1007/s00024-014-0960-2>.
- Tenzer, R., Novák, P., Vajda, P., Gladkikh, V., 2012a. Spectral harmonic analysis and synthesis of Earth's crust gravity field. *Comput. Geosci.* 16 (1), 193–207. <http://dx.doi.org/10.1007/s10596-011-9264-0>.
- Tenzer, R., Gladkikh, V., Novák, P., Vajda, P., 2012b. Spatial and spectral analysis of refined gravity data for modelling the crust–mantle interface and mantle–lithosphere structure. *Surv. Geophys.* 33 (5), 817–839. <http://dx.doi.org/10.1007/s10712-012-9173-3>.
- Tenzer, R., Novák, P., Gladkikh, V., Vajda, P., 2012c. Global crust–mantle density contrast estimated from EGM2008, DTM2008, CRUST2.0, and ICE-5G. *Pure Appl. Geophys.* 169 (9), 1663–1678. <http://dx.doi.org/10.1007/s00024-011-0410-3>.
- Tenzer, R., Pavel, N., Vladislav, G., 2012d. The bathymetric stripping corrections to gravity field quantities for a depth-dependent model of seawater density. *Mar. Geodesy* 35 (2), 198–220. <http://dx.doi.org/10.1080/01490419.2012.670592>.
- Tenzer, R., Chen, W., 2014. Regional gravity inversion of crustal thickness beneath the Tibetan plateau. *Earth Sci. Inf.* 7 (4), 265–276.
- Tenzer, R., Hamayun, K., Vajda, P., 2009. Global maps of the CRUST 2.0 crustal components stripped gravity disturbances. *J. Geophys. Res.: Solid Earth* 114 (B5). <http://dx.doi.org/10.1029/2008JB006016>.
- Tenzer, R., Novák, P., Gladkikh, V., 2011. On the accuracy of the bathymetry-generated gravitational field quantities for a depth-dependent seawater density distribution. *Stud. Geophys. Geod.* 55 (4), 609–626. <http://dx.doi.org/10.1007/s11200-010-0074-y>.
- Tenzer, R., Vajda, P., Hamayun, P., 2010. A mathematical model of the bathymetry-generated external gravitational field. *Contribut. Geophys. Geodesy* 40 (1), 31–44. <http://dx.doi.org/10.2478/v10126-010-0002-8>.
- Tikhonov, A., 1963. Solution of incorrectly formulated problems and the regularization method. *Soviet Math. Dokl.*, 5, 1035–1038.
- Tikhonov, A.N., Arsenin, V.I., 1977. *Solutions of Ill-posed Problems*, vol. 14 Winston,

- Washington, DC.
- Van der Meijde, M., Julià, J., Assumpção, M., 2013. Gravity derived Moho for South America. *Tectonophysics* 609, 456–467.
- Vinnik, L.P., Aleshin, I.M., Kaban, M.K., Kiselev, S.G., Kosarev, G.L., Oreshin, S.I., Reigber, C., 2006. Crust and mantle of the Tien Shan from data of the receiver function tomography. *Izvestiya Phys. Solid Earth* 42 (8), 639–651.
- Wittlinger, G., Vergne, J., Tappouner, P., Farra, V., Poupinet, G., Jiang, M., Paul, A., 2004. Teleseismic imaging of subducting lithosphere and Moho offsets beneath western Tibet. *Earth Planet. Sci. Lett.* 221 (1), 117–130.
- Wild-Pfeiffer, F., 2008. A comparison of different mass elements for use in gravity gradiometry. *J. Geodesy* 82 (10), 637–653. <http://dx.doi.org/10.1007/s00190-008-0219-8>.
- Zeng, R.S., Ding, Z.F., Wu, Q.J., 1994. A review of the lithospheric structures in Tibetan plateau and constraints for dynamics: *acta Geophysica Sinica* (in Chinese) 37, 99–116.
- Zeng, R.S., Teng, J.W., Li, Y.K., Klemperer, S., Yang, L.Q., 2002. Crustal velocity structure and eastward escaping of crustal material in the southern Tibet. *Sci. China* 32, 793–798.
- Zhang, Z., Deng, Y., Teng, J., Wang, C., Gao, R., Chen, Y., Fan, W., 2011. An overview of the crustal structure of the Tibetan plateau after 35 years of deep seismic soundings. *J. Asian Earth Sci.* 40 (4), 977–989.
- Zhao, W., Nelson, K.D., Che, J., Quo, J., Lu, D., Wu, C., Liu, X., 1993. Deep seismic reflection evidence for continental under thrusting beneath southern Tibet. *Nature* 366 (6455), 557–559.
- Ye, Z., Tenzer, R., Sneeuw, N., Liu, L., Wild-Pfeiffer, F., 2016. Generalized model for a Moho inversion from gravity and vertical gravity-gradient data. *Geophys. J. Int.* 207 (1), 111–128. <http://dx.doi.org/10.1093/gji/ggw251>.